Evaluating MINFLUX experimental performance *in silico*

Zach Marin[1,2], Jonas Ries[1,2,3]

[1] Max Perutz Labs, Vienna Biocenter Campus (VBC), Vienna, Austria

[2] University of Vienna, Center for Molecular Biology, Department of Structural and Computational Biology, Vienna, Austria

[3] University of Vienna, Faculty of Physics, Vienna, Austria

Abstract

MINFLUX is a super-resolution microscopy technique with remarkable resolution for imaging and tracking. Its optical resolution is well understood under idealized conditions, but because of system complexity and experimental imperfections, actual performance can be much worse.

Here we present SimuFLUX, a comprehensive and realistic simulator for MINFLUX. We use it to investigate performance limits caused by fluorophore dynamics, background, estimators, and misalignment, and to simulate experiments to optimize parameters and assess feasibility.

Introduction

MINFLUX (minimal photon flux) microscopy measures the position of single fluorophores by targeted scanning of a patterned excitation beam featuring a minimum, reaching record precision for a given number of detected photons[1–3]. MINFLUX tracking has enabled novel biological insights into the mechanisms of motor proteins[4,5], and MINFLUX imaging has reached angstrom resolution[6,7]. Technical implementations are diverse[1,2,4,8–10], but all are highly complex in data acquisition and analysis. Nowadays, commercial MINFLUX microscopes are readily accessible to many researchers at advanced imaging facilities, yet obtaining high-quality data remains challenging because of the complexity of performing a measurement and because in non-ideal biological samples numerous imperfections can cause unforeseen artifacts. How these experimental challenges impact MINFLUX quality and how they can be mitigated is still not well understood.

The theoretical limit of precision in MINFLUX has been studied extensively using the Cramér-Rao bound (CRB)[1,11,12] and Van Tree inequality calculations[13]. However, these do not include uncertainties or bias caused by imperfections stemming from optics (misalignment, aberrations), mechanics (speed of pattern scan and repositioning, vibrations), fluorophores (flickering, bleaching, movement, nearby fluorophores) or position estimators (which convert photon counts to approximate fluorophore positions) used in experiments. Simulations are needed to investigate how these imperfections influence the results, but available code can simulate only few of these confounders[1,11,12,14–16].

Here, we developed SimuFLUX, a comprehensive simulator for MINFLUX experiments. It includes realistic models of point spread functions (PSFs), fluorophores, microscope mechanics and estimators. It allowed us to answer long-standing questions on how imperfections affect MINFLUX accuracy, and we demonstrate how it can be used to optimize experimental parameters and to simulate entire experiments to judge feasibility of a project.

SimuFLUX architecture

SimuFLUX performs a detailed and realistic simulation of a MINFLUX microscope (Fig.1, Methods). The simulator scans a PSF over a sample in a defined pattern[1,2] or iterates through a set of PSFs[8] at a fixed position, measures the number of photons at each position/PSF, performs a position estimation, and then recenters the pattern by moving a fast scanner (e.g., an electro-optical deflector, EOD) and a slow scanner (a galvo[4,17] or a piezo[1,2]). The PSF model can be either experimentally calibrated[18,19] or calculated with a full vectorial PSF model that includes aberrations, misalignments, and detection through a pinhole. This allows us to simulate any MINFLUX approach, e.g. using 2D or 3D donuts or half-moon (bi-lobed) PSFs[8,20]. The fluorophore model simulates a collection of fluorophores that can switch on and off, show fast blinking (flickering) and bleaching, and can diffuse or move through defined trajectories (e.g, steps that describe moving kinesins[5] or oscillatory paths stemming from microscope vibrations). Available outputs (Figure 1c) include the raw data, localizations in a format that can be imported into SMAP[21] for further analysis, statistics on performance, the CRB, as well as tracks and images.

SimuFLUX is provided as open source in both MATLAB and Python. It is designed to be easily used by non-experts and easily extended by developers and can be run locally or remotely on Google Colab. Experiments are either defined programmatically via MATLAB scripts or Jupyter Notebooks[22] using classes in the SimuFLUX library or via text files with a syntax that is an extension of the format used in Abberior MINFLUX sequence files. This allows non-expert users to directly simulate an actual Abberior MINFLUX experiment with precise parameters, with the caveat that we replaced some propriety algorithms (e.g., the estimator), by published algorithms. All simulations in this manuscript are available as example scripts, which also serve as tutorials.

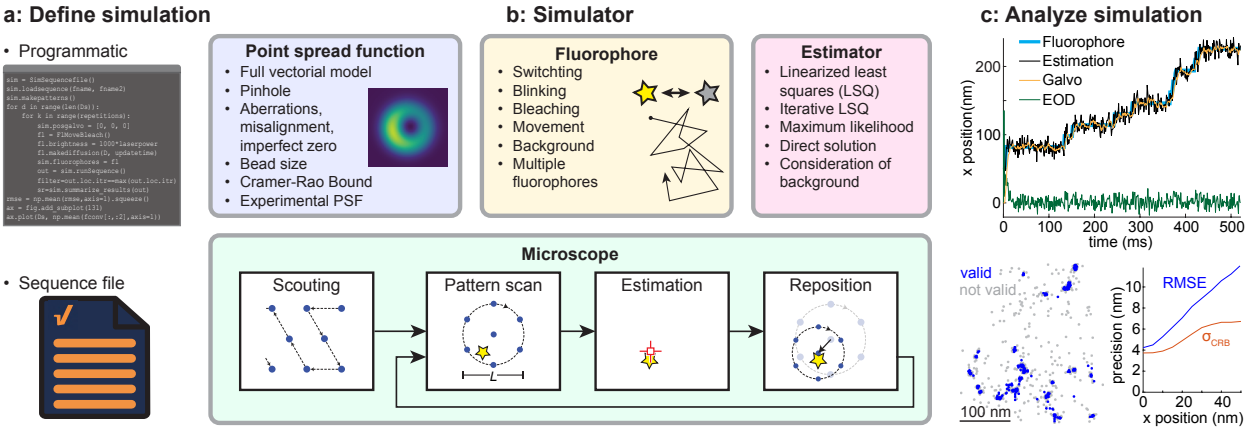

Figure 1: SimuFLUX overview. a, Simulations are defined programmatically or via sequence files. **b,** The simulator performs comprehensive simulations of a MINFLUX experiment using realistic models for the point-spread function, fluorophores, and microscope optics/software/mechanics. **c,** The output comprises raw data, simulated images, and statistics on performance.

Results

We now illustrate with several examples how SimuFLUX allows us to understand fundamental performance limitations of MINFLUX under realistic conditions, and how it helps us to develop improved MINFLUX approaches to overcome these limitations.

Careful alignment of MINFLUX optics, particularly of the phase pattern, is known to be of importance[14] and indeed we find that shifting the phase pattern by a few 100 micrometers off the optical axis (Figure 2a, Supplementary Fig. 1) results in a z-dependent bias and additional uncertainty (i.e., standard deviation) in position estimates. Note that the CRB does not reflect this deteriorated performance, highlighting the need for realistic simulations. On the other hand, a misaligned pinhole has a negligible effect on performance apart from reducing the photon detection efficiency (Supplementary Fig. 2). Aberrations and a background have a much stronger impact when using a 3D donut compared to a 2D donut or half-moon PSFs (Figure 2b, Supplementary Fig. 3). Vibrations during the measurement lead to additional uncertainties on the order of the vibration amplitude and show little frequency dependence (Supplementary Fig. 4).

A fluorescence background from nearby fluorophores, autofluorescence, or an imperfect zero of the PSF is ultimately the limiting factor for MINFLUX precision[3]. We investigated the impact of these sources of background (Supplementary Fig. 5) and found that they not only deteriorate the localization precision but also cause a strong bias of the estimator. This prompted us to develop better estimators.

Estimators must be simple and fast when run on a field-programmable gate array (FPGA) to allow for online position feedback on a sub-millisecond time scale[3]. We developed a new iterative estimator, and for 1D localizations a direct closed form estimator, which greatly extends the field of view over which there is low bias, as compared to the standard first-order estimator, while maintaining mathematical simplicity[1] (Figure 2c, Supplementary Fig. 6). We found that bias arising from background disappears if the background can be estimated precisely and is subtracted from photon counts or is used as a free fitting parameter in the estimator (Figure 2d). An estimator bias also helped us explain a phenomenon the user base experiences with the Abberior MINFLUX: often, the estimated position creeps slowly towards the true position during the first iterations, with an error of tens of nanometers. Simulations could recapitulate this behavior when the first coarse localization step was inaccurate, when beads are used that—due to their size—reduce the zero contrast, or when background estimation is imprecise (Supplementary Fig. 7).

MINFLUX assumes constant brightness during probing of positions, but fluorophores bleach and can show flickering on many time scales[23,24]. We show that flickering creates an up to tenfold increased localization error (in Figure 2e). This can be mitigated by repeated scanning; however, a high number of repetitions are needed (>20), which is not feasible with current technologies. Thus, strongly flickering fluorophores such as quantum dots should be used with care.

Next, we simulated realistic experiments for MINFLUX imaging and tracking using the default Abberior sequences.

DNA-PAINT has become increasingly popular for MINFLUX imaging because of the high photon counts detected from single fluorophores and the simplicity of sequential multi-color measurements, but the diffusing imaging strands (density ~1/μm^3) cause a background that varies

on the spatial and temporal scale of the pattern scan, potentially causing artifacts. Indeed, our simulations on the example of a nuclear pore complex[25] (Figure 2f) showed a reduced localization accuracy and many invalid localizations. Performing identical simulations with invisible imaging strands mitigated that problem (Figure 2g). Thus, DNA-PAINT with quenched imaging strands[26] might be preferable for MINFLUX, provided they do not lead to additional flickering, which remains to be investigated.

MINFLUX seems especially suited for fluorophores with a low photon budget, such as photo-activatable/photo-convertible fluorescent proteins (PAFP, as in PALM[27]). Unfortunately, in our simulations many PAFPs bleached during the scouting phase and first iterations, leading to a reduced effective labeling efficiency (Figure 2h). A simulation of organic dyes in a thiol-containing blinking buffer (as in dSTORM[28,29]) lead to a higher effective labeling efficiency and better resolution (Figure 2i).

In all these approaches, the density of activated fluorophores must be tuned carefully. At high densities, nearby active fluorophores outshine the target fluorophore close to the PSF zero and thus lead to a strong localization error (Supplementary Fig. 5g,h). Low densities further increase the already long imaging times. We thus optimized the activation density *in silico* (Supplementary Fig. 8), as a basis for experiments.

MINFLUX is especially advantageous for single fluorophore tracking, where it greatly increases the spatial and temporal resolution as well as the track length when compared to camera-based tracking[3]. However, it is difficult to track fast fluorophores, e.g., membrane diffusion with a diffusion coefficient of $D > 1$ µm^2/s. We explored the cause of this limitation by systematically investigating the impact of scan pattern shape and size, laser powers, photon limits, pattern dwell times and detection dead times on the maximal diffusion speed that can be tracked (Figure 2 j-l, Supplementary Fig. 9). We identified microscope dead times, which occur during scanner movement or during estimator calculations on the FPGA, as a main limitation and found that optimization of laser power, pattern size, photon limit and pattern dwell time increased the measurable diffusion coefficient by 70% over that captured by the standard sequence. Of note, insufficient time resolution caused an underestimation of the diffusion coefficient, thus MINFLUX diffusion measurements should be analyzed with caution.

Conclusion

SimuFLUX will be particularly useful for three directions of applications. First, it will be of use for developers, as it allows testing and optimizing new MINFLUX approaches and algorithms *in silico*. Second, it will continue to improve our theoretical understanding of MINFLUX and its dependence on various conditions. Third, we expect it to be an invaluable tool for all MINFLUX users as it will allow them to improve data quality by computationally optimizing the numerous experimental parameters, and to use realistic simulations to judge the suitability of MINFLUX to answer their biological questions before the start of a project.

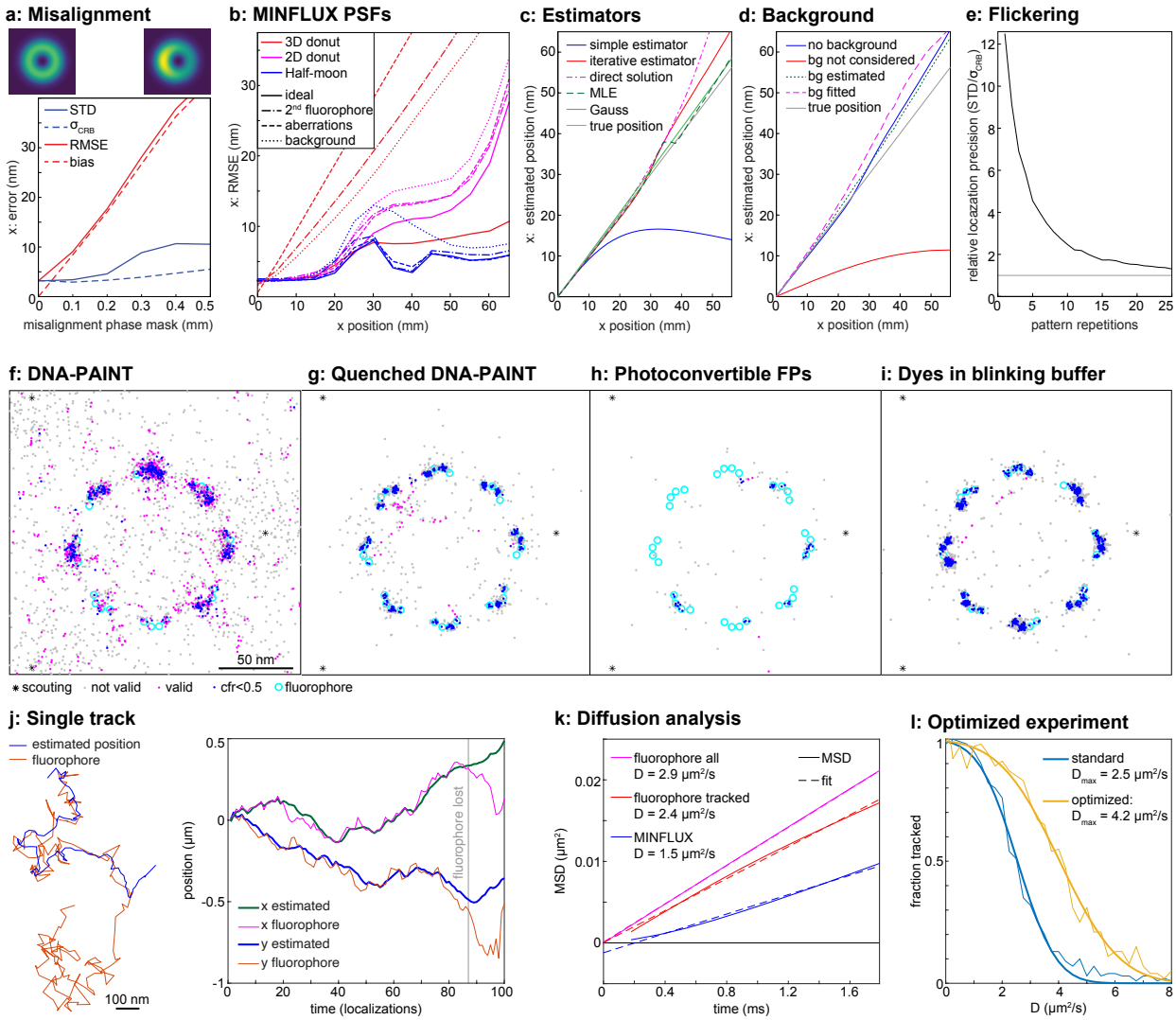

Figure 2: Simulations of MINFLUX performance in realistic experimental conditions. a, **Misalignment** of the phase mask results in a bias and increased error in position estimates (see Supplementary Fig. 1 for more details). Shown are PSFs for no misalignment and a misalignment of 0.5 mm in the sample x-direction. STD: standard deviation, RMSE: root mean square error, σ_{CRB}: localization precision from the Cramér-Rao Bound (CRB). **b, Comparison of MINFLUX PSFs**. RMSE in dependence of the field of view (x position of the fluorophore) for 2D and 3D donuts and half-moon PSFs from PhaseFLUX[8], simulated for the ideal case and in presence of background, in presence of a nearby fluorophore and with aberrations. Example PSFs are shown in Supplementary Fig. 3. **c, Estimators** (see Methods for equations) comparing the standard linearized least squares (LSQ) with an iterative LSQ estimator, a direct fit of a quadratic model, and Maximum Likelihood Estimation (MLE). The Gauss PSF was fit with a simple estimator. See Methods and Supplementary Fig. 6 for more details. 500 photons/localization. **d, Background bias** for the iterative LSQ estimator and mitigation via subtracting background from photon counts and via fitting the background. 100 signal photons, 250 background photons at x=0. **e, Fluorophore flickering.** Averaging over repeated pattern scans mitigates loss in precision. $t_{\mathrm{on}} = t_{\mathrm{off}} = 100\ \mu s$. **f-i, Comparison of different imaging modalities** on simulated nuclear pore complexes**.** MINFLUX using DNA-PAINT with standard (**f**) and fluorogenic (**g,** quenched) imaging strands, using photoconvertible fluorescent proteins (**h**, as in PALM), and organic dyes in a blinking buffer (**i**, as in dSTORM). **j-q, *In silico* optimization of MINFLUX tracking. j**, Example track of a molecule diffusing in 2D with $D = 3$ µm^2/s. When the jump of a molecule is too large (see Supplementary Fig. 9a), the microscope cannot follow, and the fluorophore is lost. **k**, The limited time resolution in combination with loss of fast dynamics leads to an underestimation of the diffusion coefficient in MINFLUX and non-linear mean square displacement (MSD) over time. **l,** A systematic optimization of laser power, pattern size, photon limit and pattern dwell time allowed us to substantially increase the time resolution. 90 consecutive localizations were considered a successful track, $D_{\max}$ denotes the diffusion coefficient for which half of the tracks were successful.

Methods

Software practices

This software is open source, released under the GNU General Public License v3.0. We welcome contributions from the community.

Complete versions of this simulator are written in both MATLAB and Python. While MATLAB is by default easy to install and use, inconsistencies in Python package management can often make dissemination of software difficult. To ensure the software is easy to install, we minimized the dependencies of the Python library. Only numpy[30] and scipy[31] are required to run the software, and IPython/Jupyter notebooks[22] are needed to interact with the software via the example notebooks. We also published the Python notebooks on Google Colab to allow researchers to use the simulator without installing anything.

The software is written using an object-oriented programming paradigm, with parts of the microscope and sample (described below) implemented as distinct classes for clear, logical separation of behavior and tasks. Because of this application programming interface, this simulator could be incorporated into popular third party software such as napari[32].

Microscope model

The microscope is implemented as a point-scanning system with a descanned large range 'slow' scanner (a galvo[4,17] or a piezo[1,2] for x-y scanning and optionally a deformable mirror for z-scanning[17]) and optionally a 'fast' scanner (e.g., an electro-optical deflector, EOD), which only affects the excitation path, i.e., it is not descanned in detection, in line with current implementations[1,2,4,8–10]. Excitation positions and timings of these scanners can be controlled from the "posgalvo" and "posEOD" properties of the "Simulator" class. The excitation profile is defined by a point spread function (PSF), or a collection of PSFs, which are implemented as children of the "Psf" class (see PSF model for details). Photon collection is assumed to be proportional to the PSF excitation intensity multiplied by the PSF detection efficiency, with the pinhole centered onto the pattern center, as the fast scanner is not descanned in the detection arm. The collected intensity is governed by a "Fluorophore" class or child "intensity" function. Aberrations and optical misalignment are modeled in the PSF. System vibrations can be modeled using moving fluorophores ("FlMoving" class or children).

Experiment model

MINFLUX experiments are established *in silico* via the "Simulator" class, which takes a microscope model, a single fluorophore or a collection of fluorophores, one or more patterns, an estimator, and feedback on the scan position. Patterns are generated as a series of PSF positions, using the "definePattern" function in the "Simulator" class or a collection of PSFs. Sequences are lists of "Simulator" patterns and components (e.g. estimators) that can tell the simulator to run patterns, collect signal, use an estimator to evaluate fluorophore positions, update the scanner positions, and repeat.

In the “Simulator” class, each fluorophore position is probed with the full sequence provided to the simulator.

Abberior MINFLUX model

The “SimSequencefile” class extends the “Simulator” class to allow users to load Abberior sequence files and simulate their behavior. These sequence files can be adapted to simulate any other MINFLUX microscopes.

Abberior sequences files contain a list of MINFLUX scanning iterations and their properties, as well as global parameters shared across all iterations. Because Abberior estimators are proprietary, we also include a custom JSON file (defaultestimators.json) that complements Abberior sequences files and indicates which estimators are used after each Abberior iteration. This file pulls from estimators implemented in as functions in the “estimators” folder. Once files are loaded, patterns (from “definePattern”, described above) are generated for each iteration.

For each simulated experiment, first, a scouting pattern formed by moving the excitation PSF over the field of view in a hexagonal grid is used to identify candidate positions of fluorophores (scouting in Figure 2f-i and Supplementary Figure. 8 legends). Any position eliciting signal is marked as a candidate. Each candidate fluorophore is probed until the photon limit (“phtLimit”) is reached, until it is bleached or lost (collected photons below “bgcThreshold”) or, in case of probing the pattern center, until it fails the CFR check. The CFR is the ratio of the signal collected when illuminating a point at the centroid of a scanning pattern to the average signal of the rest of the pattern. CFR check fails if the CFR value is greater than the parameter “ccrLimit”. Both CFR check and brightness check can fail for the number of times defined by the “stickiness” parameter. Localizations that pass the photon threshold or CFR checks are marked as valid, while those that do not pass either of these checks are marked as invalid (e.g., in Figure 2f-i and Supplementary Fig. 8).

Additional filtering of the CFR value allows for rejecting poor localizations (e.g. cfr<0.5 in Figure 2f-i and Supplementary Fig. 8), for example caused by nearby fluorophores or a large offset between fluorophore and pattern center.

The “SimSequencefile” class currently understands the Abberior iteration specific parameters “ccrLimit”, “pattern”, “patDwellTime”, “patRepeat”, “pwrFactor”, “patRepeat”, “maxOffTime”, “phtLimit”, and “wavelength”, and the global parameters “bgcThreshold”, “ctrDwellFactor”, “damping”, “headstart”, “id”, “loclimit”, “stickiness”, and “fieldGeoFactor” from the “field” structure. These parameters are described in detail in an annotated YAML file (Tracking_2D.yaml, uploaded to GitHub, see Code Availability section) derived from an Abberior JSON sequence file. The “algo” setting from the “field” structure currently only performs scouting for fluorophores by scanning a Gaussian beam in a hexagonal grid (“hexgrid”) pattern, but this could be easily extended to other search patterns in the “makescoutingpattern” class function.

PSF model

PSFs models are implemented as derivates of the “Psf” class, with each child class containing different methods to express PSF shape. PSF profiles can be expressed analytically, as in the

“PsfGauss2D” and “PsfDonut2D” classes, or via a vectorial PSF model (“PsfVectorial” class) based on Leutenegger et al.[20]. The “PsfVectorial” class calculates the electromagnetic field using fast Fourier transforms by taking the vectorial Debye diffraction integral. For the different beam shapes, the phase patterns of the input beam at the back focal plane can be modified via the “phasepattern” argument to the “calculatePSFs” function in the “PsfVectoral” class, simulating use of e.g. a spatial light modulator. We additionally introduced a pinhole (controlled via the “setpinhole” function), which can be misaligned via a shift (see Supplementary Fig. 2). Multiplication of the excitation PSF at a specific pattern position by a detection PSF through a pinhole at the pattern center is used to simulate the effects of both the excitation and detection PSFs in the optical system. We also introduce a bead size parameter (controlled via the “beadsize” function) that, when set to greater than zero, will result in a bead being convolved with the PSF. Large beads introduce an apparent background into the PSF shape by averaging out the zero, which can be useful for simulating the source of tracking errors (see Supplementary Fig. 7).

Default parameters for the vectorial PSF – including, but not limited to magnification, numerical aperture, refractive index of the immersion solution and the sample, pixel size, and aperture diameter – can be found, with descriptions, in the “default_microscope.yaml” file included with the software. This file is loaded, and its parameters are applied by default when generating a vectorial PSF.

Finally, experimentally calibrated PSFs[18,19] can be directly loaded (“PsfVectorial” class), combined with pinhole detection, and used for simulations.

Fluorophore model

Individual fluorophores are implemented as children of the “Fluorophore” class, with changes to position (“position” function) and intensity (“intensity” function) modeled as needed in, e.g., fluorophores that move (“FIMoving” class) and those that bleach (“FIBleach” class). Collections of fluorophores, which can model everything from multiple diffusing particles to fixed nuclear pore complexes, are implemented using the “FICollection” class and its children.

Moving fluorophores provide the coordinates at defined time points t_i via the “position” function. Positions can be defined as mathematical functions, or by directly providing the position $x_i(t_i)$ on a sufficiently dense time axis. Note that currently each point measurement is performed at a fixed fluorophore position, thus the time resolution dt should be below the point detection time. Finer sampling can be implemented by probing each point several consecutive times.

Tracks for specific motions can be pre-calculated.

Diffusion is modeled by generating jump lengths W_k for each coordinate k from a normal distribution:

$$W_k = \sqrt{2\,D\,dt} \cdot \text{randn}(\,) \tag{1}$$

where dt is the simulated time window length and D (μm^2/s) is the diffusion coefficient. The position of a fluorophore at time t_i is the cumulative sum of the jumps that occurred until this time point.

Stepping was modeled by generating the time interval between steps from an exponential distribution with a mean equal to the step dwell time t_{step}. Steps were then sampled with the simulated time window length dt, and the step position at time t_i was the cumulative sum of the steps that occurred until this time point.

Fluorophores in "FlBleach" were initialized with a total number of photons set to a random number taken from an exponential distribution with a mean equal to a specified mean number of photons. To model bleaching, the number of detected photons in a measurement was subtracted from this total until it reduced to zero. Note that we subtracted the number of photons before application of the pinhole, as these correspond to the emitted photons.

Blinking was modeled in "FlBlinkBleach" by using random exponential distributions for the on and off times of the fluorophore, with means t_{on} and t_{off}, respectively, to pre-calculate the emission state over time as the time of on- and off-switching events. The "measure" function calculates the fraction of the measurement time window during which the fluorophore was in its on-state and this "measure" function is called by the "intensity" function to calculate the total number of fluorophores emitted in a time window.

Estimators

Estimators are functions that take positions of an excitation PSF and the fluorophore intensity response as inputs and return an estimation of the fluorophore's position. Here we consider simple estimators that can potentially be deployed on an FPGA for real-time feedback on the scanning position. Estimators can be evaluated as part of the simulator's sequence by defining them as a "Simulator" class component via its "defineComponent" function.

Here, we follow Balzarotti et al.[1]. Typically, we perform K measurements with the PSF $f(\boldsymbol{x})$ positioned at $\boldsymbol{b}_i$ for $i \in K$. For 2D or 3D measurements $\boldsymbol{b}_i$ is a vector. Then the expected number of detected photons in each position is

$$I_i = I_0(f(\boldsymbol{x} - \boldsymbol{b}_i) + bg). \tag{2}$$

where I_0 describes fluorophore brightness and laser intensity, and bg denotes a fluorescent background. The probability of measuring a fluorophore with the illumination profile is defined as

$$p_i = \frac{I_i}{\sum_{j=1}^{K} I_j}. \tag{3}$$

Note that any PSF normalization factor, as well as I_0, cancel out.

The estimation task consists of estimating $\boldsymbol{x}$ from experimentally measured photon numbers $\hat{n}_i$ with $\widehat{N} = \sum \hat{n}_i$ being the total number of detected photons, or from the measured probabilities $\hat{p}_i = \hat{n}_i / \widehat{N}$.

In the following we will review common estimators from the literature[1] and derive our own estimators (see the accompanying Mathematica notebook SimuFLUX_estimators.nb).

Linearized Least Squares Estimator

The least squares (LSQ) estimator minimizes

$$S = \sum_i (\hat{n}_i - I_i)^2 = \sum_i (\hat{p}_i - p_i)^2 \,. \tag{4}$$

Note that we can use the background-free case, if we subtract the background from $\hat{n}_i$:

$$S = \sum_i ((\hat{n}_i - I_0 bg) - I_0 f(\boldsymbol{x} - \boldsymbol{b}_i))^2 \tag{5}$$

Thus, in the following we will not consider the background. A common approach to solving an LSQ problem is to linearize $p(\boldsymbol{x})$. Linearization around $\boldsymbol{x} = 0$ results in the simple estimator (see Balzarotti et al.[1], Eq. S43-S48):

$$\boldsymbol{x}_{\text{est}} = (J^T J)^{-1} J^T \big(\hat{\boldsymbol{p}} - \boldsymbol{p}(0)\big), \tag{6}$$

where $J = \partial p_i / \partial x_j$ is the Jacobian matrix.

The PSF (integral normalized to A) of a MINFLUX donut can be approximated as[1]:

$$f_d(\boldsymbol{x}) = A \, \frac{\boldsymbol{x}^2}{4\,\pi\,\sigma^4} \, e^{-\frac{\boldsymbol{x}^2}{2\sigma^2}}, \tag{7}$$

With $L_\sigma^2 = L^2/8\sigma^2$, the linearized least squares estimator for the donut is[1]:

$$\boldsymbol{x}_{\text{est}} = \frac{1}{L_\sigma^2 - 1} \sum_i \hat{p}_i \, \boldsymbol{b}_i. \tag{8}$$

Derived for $K = 3$ measurement positions in an orbit of diameter L, this estimator is also a good estimator for more measurement points. Because of the expansion around $\boldsymbol{x} = 0$ it becomes biased when the fluorophore is not at the center of the scan pattern. Balzarotti et al. debiased this estimator, however, and this only works in a relatively small range around $\boldsymbol{x} = 0$.

The center of the donut can be approximated by a quadratic function (first order approximation of eq. 7):

$$f_q(\boldsymbol{x}) = \mathrm{A} \frac{\boldsymbol{x}^2}{4\pi\sigma^4}. \tag{9}$$

where σ describes the steepness of the PSF. As can be seen in Supplementary Fig. 6, this approximation is very good in the range of interest, i.e., when $|\boldsymbol{x}| < L/2$. The linearized LSQ solution for the quadratic PSF is:

$$\boldsymbol{x}_{\text{est}} = -\sum_i \hat{p}_i \, \boldsymbol{b}_i. \tag{10}$$

For a Gaussian PSF,

$$f_q(\boldsymbol{x}) = \mathrm{A}\, e^{-\frac{\boldsymbol{x}^2}{2\sigma^2}}, \tag{11}$$

the linearized LSQ estimator around $\boldsymbol{x} = 0$ is (see SimuFLUX_estimators.nb):

$$\boldsymbol{x}_{\text{est}} = \frac{1}{L_\sigma^2} \sum_i \hat{p}_i \, \boldsymbol{b}_i \tag{12}$$

if the center is not measured, and

$$\boldsymbol{x}_{\text{est}} = \left(K_o + e^{L_\sigma^2}\right)\frac{1}{K_o L_\sigma^2}\sum_i \hat{p}_i\, \boldsymbol{b}_i \tag{13}$$

if the center is measured (K_o is the number of points in the circular orbit).

Iterative Least Squares Estimator

To extend the range of the LSQ estimators, we can linearize p_i around an arbitrary location $\boldsymbol{x}_0$ to calculate the Jacobian J_{x0} at this location and use $\boldsymbol{x}_0$ and J_{x0} in Eq. 6.

In an iterative approach, starting with $\boldsymbol{x}_0 = 0$, in every iteration we can set $\boldsymbol{x}_{0,i} = \boldsymbol{x}_{\text{est},i-1}$. This estimator converges within a few iterations (Supplementary Fig. 6). In the accompanying Mathematica notebook (SimuFLUX_estimators.nb), we calculated the Jacobian J_{x0} analytically for $K_o = 3$, $K_o = 4$ and $K_o = 6$ probing positions at the orbit, with and without probing the pattern center.

Other estimators for 1D localization

For the 1D case, we can derive simple analytical estimators either as a maximum likelihood estimator (MLE) or using a direct solution of a system of equations by equating measurements with the theoretical probabilities and solving for the position. Both approaches are relevant also for 2D or 3D MINFLUX measurements, as often two measurements on opposing sides of the orbit, with or without center measurement, can be treated as a 1D measurement. Also, implementations like the interferometric MINFLUX[4] or PhaseFLUX[8] consist of sequential 1D measurements for each coordinate.

The maximum likelihood estimator (MLE) for the quadratic PSF with probing points at $b_i = [-L/2, L/2]$ has been derived by Balzarotti et al.[1]:

$$x_{\text{est},1} = \frac{L}{2}\frac{\sqrt{\hat{n}_1} - \sqrt{\hat{n}_2}}{\sqrt{\hat{n}_1} + \sqrt{\hat{n}_2}}\,, \qquad x_{\text{est},2} = \frac{L}{2}\frac{\sqrt{\hat{n}_1} + \sqrt{\hat{n}_2}}{\sqrt{\hat{n}_1} - \sqrt{\hat{n}_2}}. \tag{14}$$

A center measurement $\hat{n}_0$ can be used to calculate the likelihood for both solutions to choose the correct one.

For $K = 2$ we can directly solve the equations

$$\hat{p}_{\boldsymbol{i}} == p(b_i) \tag{15}$$

for x and I_0. Interestingly, for the quadratic approximation, this solution is identical to the MLE solution (Eq. 14, see SimuFLUX_estimators.nb).

For $K = 3$, i.e., three measurements $\hat{n}_0, \hat{n}_1, \hat{n}_2$ at $b_i = [0, -L/2, L/2]$, we can solve for x, I_0 and the background bg, i.e., treat the background as a free fitting parameter, instead of calibrating it with a separate measurement. Then, the estimated position is,

$$x_{est} = \frac{L}{4}\frac{\hat{n}_2 - \hat{n}_1}{2\hat{n}_0 - \hat{n}_1 - \hat{n}_2}. \tag{16}$$

Data analysis

Cramér-Rao bounds (CRBs) for each PSF were calculated numerically following the framework in Masullo et al.[11]: the Fisher information matrix was computed from the derivatives of the normalized PSF patterns and inverted to compute the lower bound. To get the Fisher information matrix, we first evaluated the pattern scan for each fluorophore at position $\boldsymbol{x} - \varepsilon/2$ and $\boldsymbol{x} + \varepsilon/2$ and then computed the numerical derivative for each axis. We then use the product of these derivatives pairwise to compute the Fisher information matrix such that it contains all information from the simulation, including background, the presence of other fluorophores, and aberrations in the scan PSF.

In addition to using the CRB, the success of experiments was evaluated on the following metrics.

The root mean squared error (RMSE) was defined as

$$\mathrm{RMSE} = \frac{1}{Q}\sum_{i=1}^{Q}(\hat{x}_i - x_i)^2 \tag{17}$$

where Q was the total number of fluorophores in the sample, $\hat{x}_i$ was the estimated position of the fluorophore and x_i was the true position of the fluorophore.

The standard deviation (STD) was defined as

$$\mathrm{STD} = \sqrt{\frac{1}{Q}\sum_{i=1}^{Q}|(\hat{x}_i - x_i) - \bar{x}|^2} \tag{18}$$

where Q was the total number of fluorophores in the sample, $\hat{x}_i$ was estimated position of the fluorophore, x_i was the true position of the fluorophore, and $\bar{x} = \frac{1}{Q}\sum_{i=1}^{Q}(\hat{x}_i - x_i)$.

The bias was defined as

$$\mathrm{bias} = \bar{x} = \frac{1}{Q}\sum_{i=1}^{Q}(\hat{x}_i - x_i) \tag{19}$$

where Q was the total number of fluorophores in the sample, $\hat{x}_i$ was estimated position of the fluorophore, and x_i was the true position of the fluorophore.

Code availability

Source code is available under a GPLv3 license at https://github.com/ries-lab/SimuFLUX/.

Acknowledgements

We thank Nikolay Sergeev, Sha Hao and Dr. Ioannis Pitsios for testing this software. We thank Dr. Sarah Schweighofer, Nikolay Sergeev, Dr. Takahiro Deguchi, Dr. Ioannis Pitsios, and Dr. Francesco Reina for manuscript feedback. This work was supported by the European Research Council (ERC CoG-724489, PoC-101199020 to J.R.).

References

1. Balzarotti, F. *et al.* Nanometer resolution imaging and tracking of fluorescent molecules with minimal photon fluxes. *Science* **355**, 606–612 (2017).
2. Gwosch, K. C. *et al.* MINFLUX nanoscopy delivers 3D multicolor nanometer resolution in cells. *Nat. Methods* **17**, 217–224 (2020).
3. Scheiderer, L., Marin, Z. & Ries, J. MINFLUX achieves molecular resolution with minimal photons. *Nat. Photonics* **19**, 238–247 (2025).
4. Wirth, J. O. *et al.* MINFLUX dissects the unimpeded walking of kinesin-1. *Science* **379**, 1004–1010 (2023).
5. Deguchi, T. *et al.* Direct observation of motor protein stepping in living cells using MINFLUX. (2023).
6. Sahl, S. J. *et al.* Direct optical measurement of intramolecular distances with angstrom precision. *Science* **386**, 180–187 (2024).
7. Hensel, T. A., Wirth, J. O., Schwarz, O. L. & Hell, S. W. Diffraction minima resolve point scatterers at few hundredths of the wavelength. *Nat. Phys.* **21**, 412–420 (2025).
8. Deguchi, T. & Ries, J. Simple and robust 3D MINFLUX excitation with a variable phase plate. *Light Sci. Appl.* **13**, 134 (2024).
9. Cole, F. *et al.* Super-resolved FRET and co-tracking in pMINFLUX. *Nat. Photonics* (2024) doi:10.1038/s41566-024-01384-4.
10. Geismann, M. K., Gomez-Segalas, A., Passera, A., Shirzadian, M. & Balzarotti, F. A Fast Interferometric Beam Shaper for Multi-Emitter 3D MINFLUX. *bioRxiv* 2023.12.09.570565 (2024) doi:10.1101/2023.12.09.570565.
11. Masullo, L. A., Lopez, L. F. & Stefani, F. D. A common framework for single-molecule localization using sequential structured illumination. *Biophys. Rep.* **2**, 100036 (2022).
12. Liu, Y., Dong, J., Augusto Maya, J., Balzarotti, F. & Unser, M. Point-spread-function engineering in MINFLUX: optimality of donut and half-moon excitation patterns. *Opt. Lett.* **50**, 37–40 (2025).
13. Kalisvaart, D. *et al.* Precision in iterative modulation enhanced single-molecule localization microscopy. *Biophys. J.* **121**, 2279–2289 (2022).
14. He, C. *et al.* Effects of optical aberrations on localization of MINFLUX super-resolution microscopy. *Opt. Express* **30**, 46849–46860 (2022).
15. Slenders, E. & Vicidomini, G. ISM-FLUX: MINFLUX with an array detector. *Phys Rev Res* **5**, 023033 (2023).
16. Masullo, L. A. *et al.* Pulsed Interleaved MINFLUX. *Nano Lett.* **21**, 840–846 (2021).
17. Schmidt, R. *et al.* MINFLUX nanometer-scale 3D imaging and microsecond-range tracking on a common fluorescence microscope. *Nat. Commun.* **12**, 1478 (2021).
18. Liu, S. *et al.* Universal inverse modeling of point spread functions for SMLM localization and microscope characterization. *Nat. Methods* **21**, 1082–1093 (2024).
19. Li, Y. *et al.* Real-time 3D single-molecule localization using experimental point spread functions. *Nat. Methods* **15**, 367–369 (2018).
20. Leutenegger, M., Rao, R., Leitgeb, R. A. & Lasser, T. Fast focus field calculations. *Opt. Express* **14**, 11277–11291 (2006).
21. Ries, J. SMAP: a modular super-resolution microscopy analysis platform for SMLM data. *Nat. Methods* **17**, 870–872 (2020).
22. Kluyver Thomas *et al.* Jupyter Notebooks – a publishing format for reproducible computational workflows. in *Positioning and Power in Academic Publishing: Players, Agents and Agendas* (IOS Press, 2016). doi:10.3233/978-1-61499-649-1-87.
23. Huang, Z. *et al.* Spectral Identification of Specific Photophysics of Cy5 by Means of Ensemble and Single Molecule Measurements. *J. Phys. Chem. A* **110**, 45–50 (2006).

24. Widengren, J. & Schwille, P. Characterization of Photoinduced Isomerization and Back-Isomerization of the Cyanine Dye Cy5 by Fluorescence Correlation Spectroscopy. *J. Phys. Chem. A* **104**, 6416–6428 (2000).
25. Thevathasan, J. V. *et al.* Nuclear pores as versatile reference standards for quantitative superresolution microscopy. *Nat. Methods* **16**, 1045–1053 (2019).
26. Chung, K. K. H. *et al.* Fluorogenic DNA-PAINT for faster, low-background super-resolution imaging. *Nat. Methods* **19**, 554–559 (2022).
27. Betzig, E. *et al.* Imaging Intracellular Fluorescent Proteins at Nanometer Resolution. *Science* **313**, 1642–1645 (2006).
28. Rust, M. J., Bates, M. & Zhuang, X. Sub-diffraction-limit imaging by stochastic optical reconstruction microscopy (STORM). *Nat. Methods* **3**, 793–796 (2006).
29. Heilemann, M. *et al.* Subdiffraction-resolution fluorescence imaging with conventional fluorescent probes. *Angew. Chem. Int. Ed.* **47**, 6172–6176 (2008).
30. Harris, C. R. *et al.* Array programming with NumPy. *Nature* **585**, 357–362 (2020).
31. Virtanen, P. *et al.* SciPy 1.0: fundamental algorithms for scientific computing in Python. *Nat. Methods* **17**, 261–272 (2020).
32. Sofroniew, N. *et al.* napari: a multi-dimensional image viewer for Python. Zenodo https://doi.org/10.5281/zenodo.15029515 (2025).

Supplementary Figures

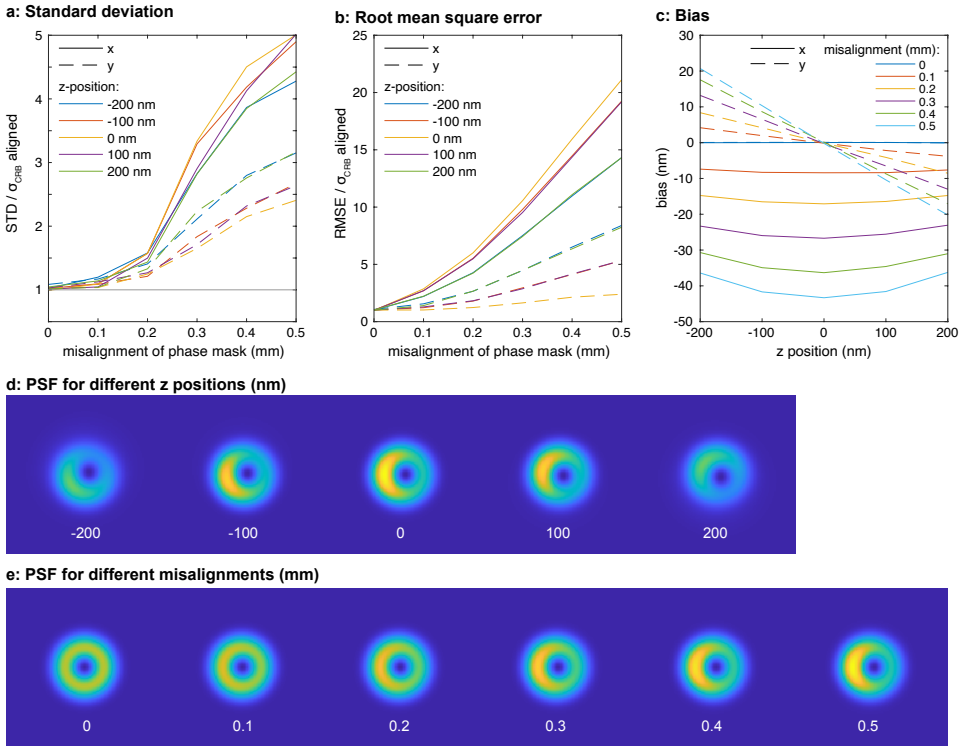

Supplementary Fig. 1. Misalignment of the vortex phase pattern. Simulation of how a misalignment of a vortex phase pattern along the x-direction affects fluorophore localization. **a,** The ratio of the standard deviation (STD, see Data Analysis section of Methods) of the fluorophore's position estimate to the Cramér-Rao Bound (CRB) for a perfectly aligned phase pattern as a function of misalignment, investigated for fluorophores at varying distances from the focal plane. Misalignment has the greatest effect on STD in the direction of misalignment. **b,** The normalized root mean square error (RMSE, see Methods) of the true and estimated fluorophore position as a function of misalignment. **c,** Bias (see Methods) of the estimated fluorophore position as a function of the fluorophore's distance from the focal plane. **d,** The point spread function (PSF) at different z positions. **e,** The PSF at the plane of focus (z=0) for misalignments in steps of 0.1 mm. For all plots, L=75 nm, vortex phase mask, a scan pattern consisting of 6 orbit plots plus their centroid, point dwell time of 0.1 ms, average photons (aligned case) of 45 per localization, iterative position estimator. See example 2c (example2c_phaseplate_misalignment.m or .ipynb).

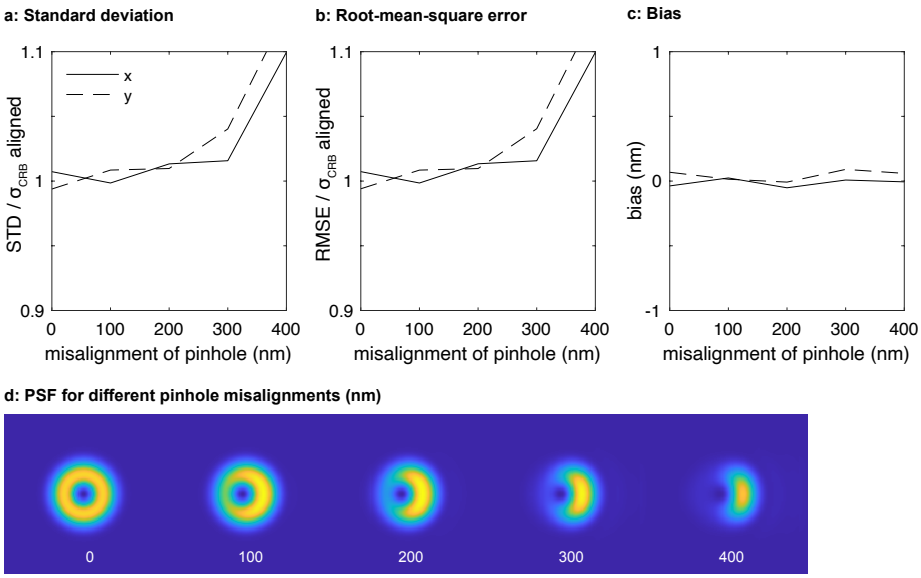

Supplementary Fig. 2. Misalignment of the pinhole. Simulation of how a misalignment of the pinhole along the x-direction affects fluorophore localization. **a,** The ratio of the standard deviation (STD, see Data Analysis section of Methods) of the fluorophore's position estimate to the Cramér-Rao Bound (CRB) for a perfectly aligned pinhole as a function of misalignment. Misalignment has limited effect on STD. **b,** The normalized root mean square error (RMSE, see Methods) of the true and estimated fluorophore position as a function of pinhole misalignment. Misalignment has limited effect on RMSE. **c,** Bias (see Methods) of the estimated fluorophore position as a function of pinhole misalignment. There is no effect. **d,** The PSF at the plane of focus (z=0) for pinhole misalignments in steps of 0.1 mm. For all plots, L=75 nm, vortex phase mask, a scan pattern consisting of 6 orbit plots plus their centroid, point dwell time of 0.1 ms, average photons (aligned case) of 72, iterative position estimator. See example 2d (example2d_pinhole_misalignment.m or .ipynb).

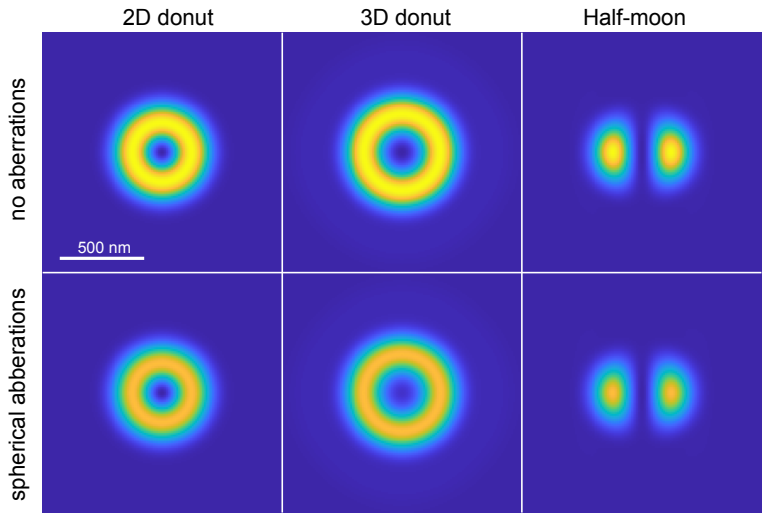

Supplementary Fig. 3. Aberrations. Effects of spherical aberrations on 2D and 3D (top hat phase mask) donut (vortex phase mask) and phase flux (halfmoon phase mask) point spread functions, shown in the plane of focus. Spherical aberrations applied are 0.15 rad.

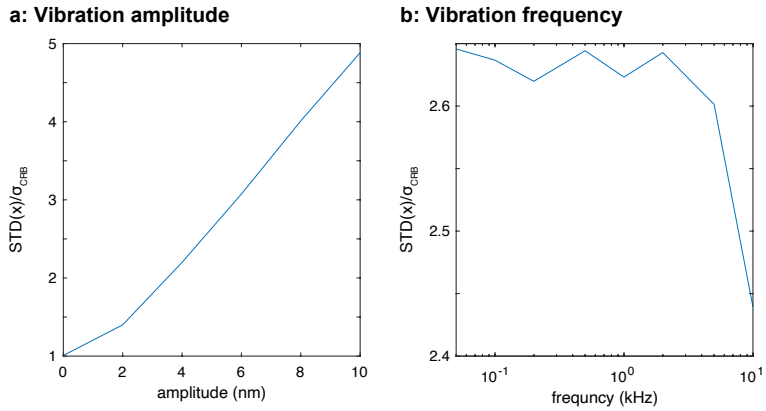

Supplementary Fig. 4. System Vibrations. The effect of system vibrations on standard deviation of fluorophore position estimate (STD, see methods). Vibrations were simulated using moving fluorophores ("FlMoving" class, see Methods). **a,** Fluorophores oscillating at a frequency of 100 Hz with varying amplitudes. Increased amplitude leads to decreased precision in fluorophore position. **b,** Fluorophores moving at varying frequences with an amplitude of 5 nm. STD has low dependence on frequency. In all experiments, fluorophores were localized with the 2D tracking sequence, Tracking_2D.json. See example 5 (example5_moving_fluorophore.m or .ipynb).

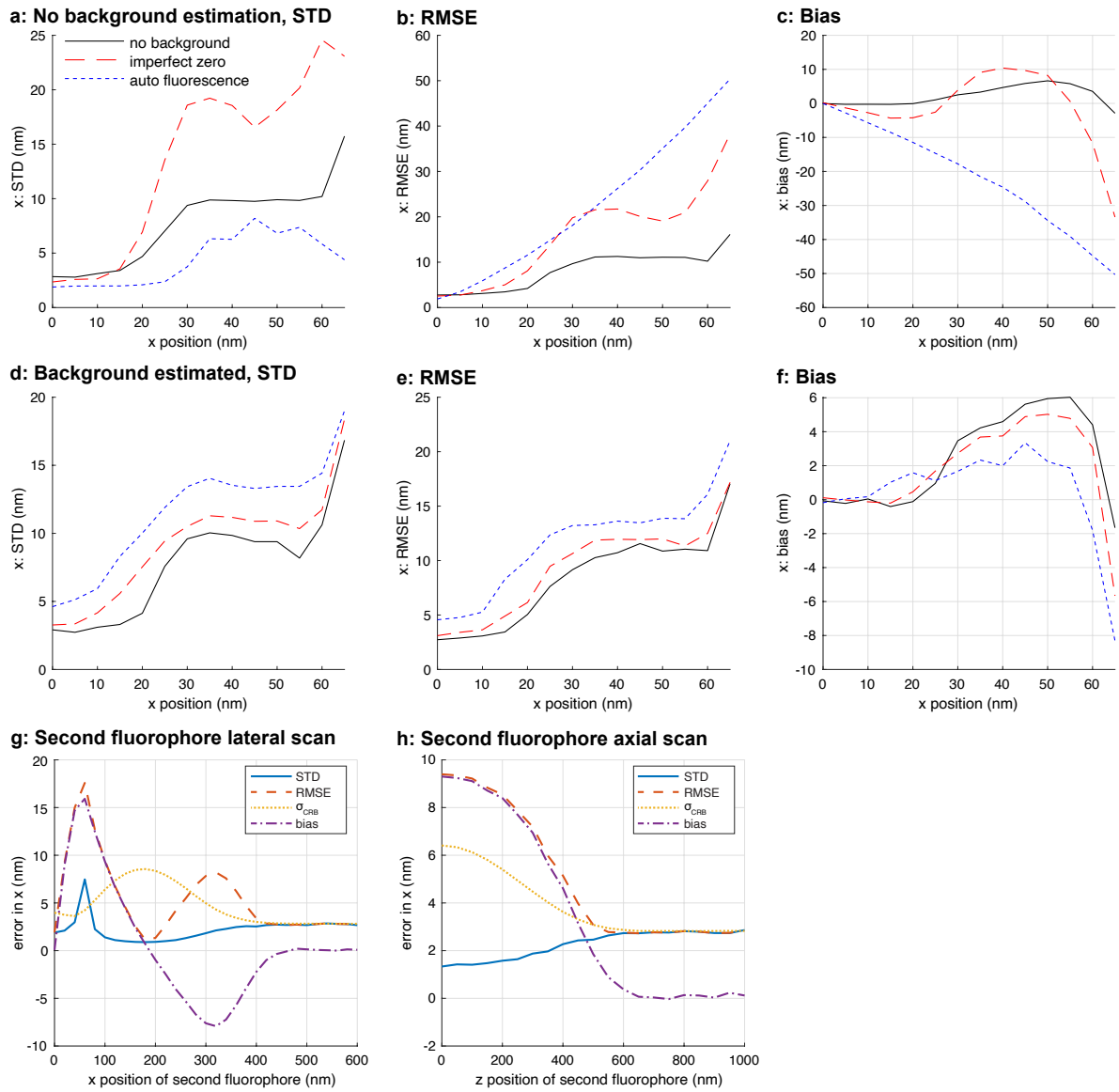

Supplementary Fig. 5. Background. Effects of background from imperfect zero, from autofluorescence, and from nearby fluorophores on emitter localization. **a-c,** The background is not considered, which leads to a bias in the iterative quadratic LSQ estimator. **d-f,** The background is estimated and subtracted from the photon counts before estimation, which removes the bias. The background still causes an increased localization error (STD). **g-h,** Effect of a nearby fluorophore of equal brightness.

Background values: Zero-offset (psf.zerooffset): 0.01; auto fluorescence background (sim.background): 30 kHz. L=75 nm. Position of the target fluorophore: [0,0,0]. Position of nearby fluorophore at [50 50 400] nm unless otherwise indicated. 100 photons/localization (no background case). See example 8 (example8_background.m or .ipynb).

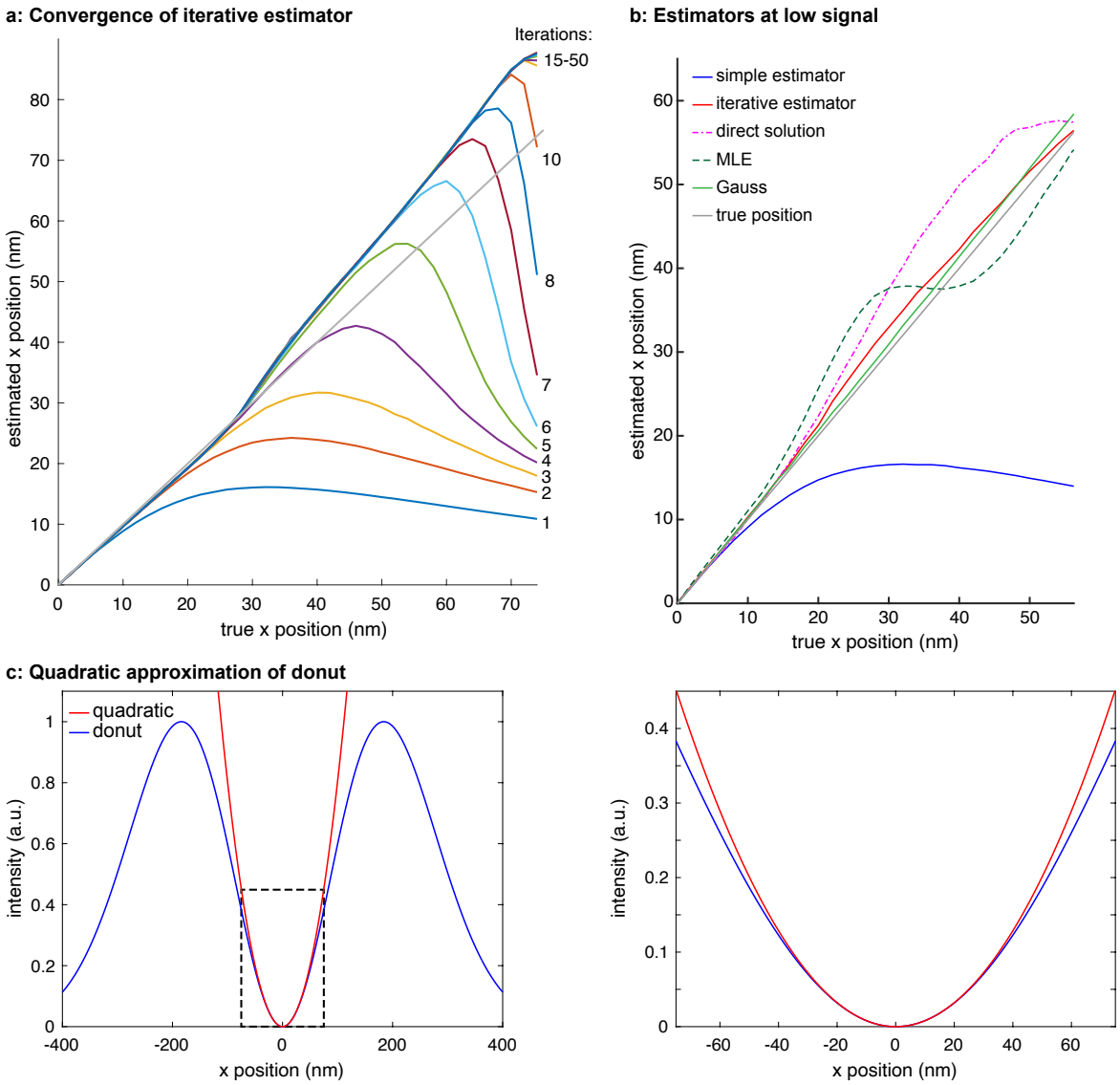

Supplementary Fig. 6. Estimators. a, Convergence of the iterative estimator with a quadratic approximation (Methods, Eq. 16) over repeated scans of a fluorophore with a donut-shaped point spread function. As the number of iterations increases, the estimated x position converges to the true estimated position over a larger field of view, with some bias after 30 nm due to mismatches between the quadratic approximation of the excitation PSF and the donut excitation, shown in **c**. **b,** The performance of various estimators, described in Methods, with only 15 signal photons collected. The iterative estimator and the Gaussian approximation via least squares perform best in these low light level conditions. Notably, the maximum likelihood estimate (MLE) has the strongest bias for low photon counts. **c,** A plot of a donut shape and its quadratic approximation. Note that the quadratic approximation only matches the donut near x=0 nm. Right shows the left black dashed box zoomed in for detailed comparison. Estimators using a quadratic approximation of a donut fail when the fluorophore is not near the donut center.

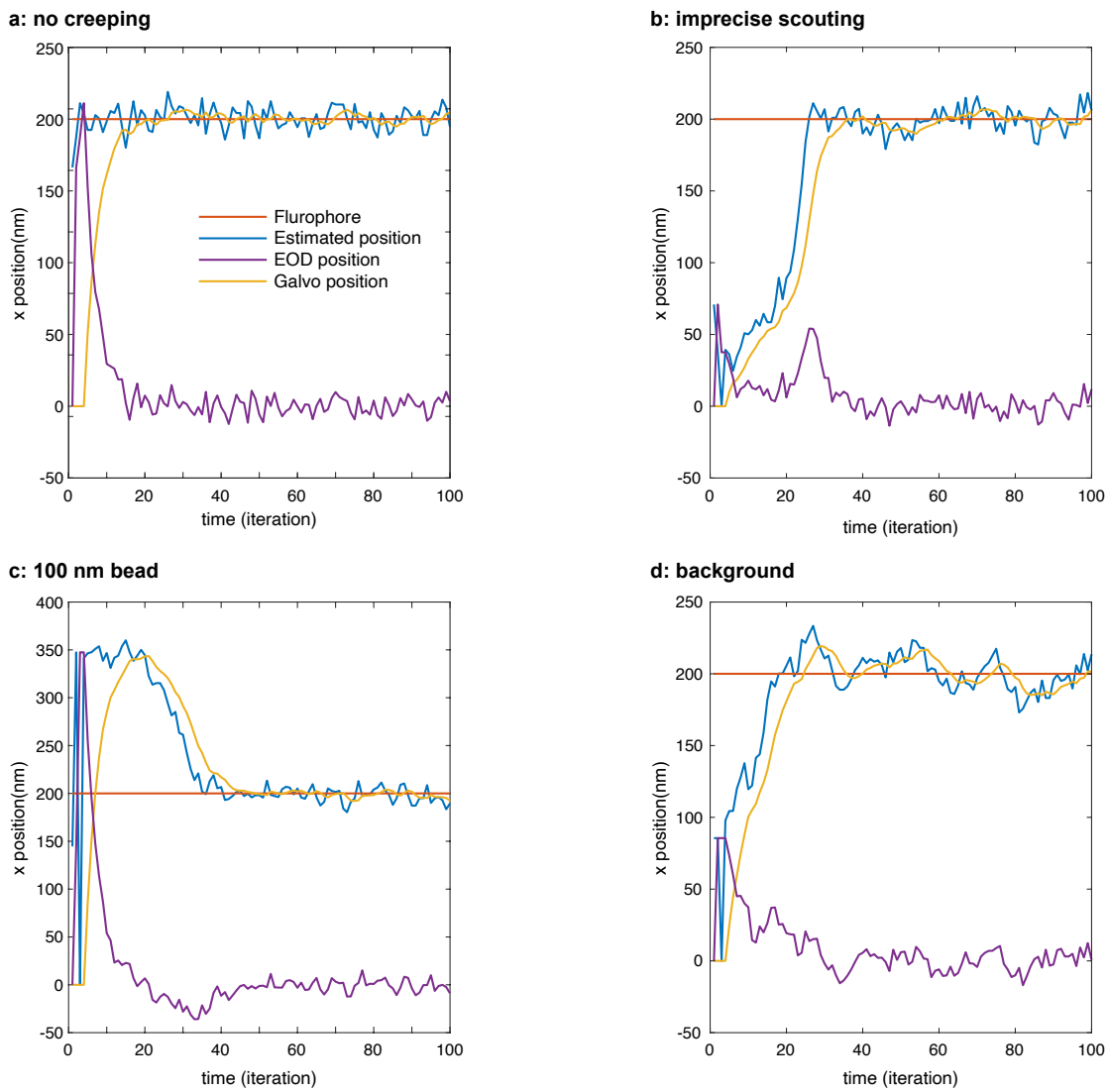

Supplementary Fig. 7. Creeping of estimated fluorophore position. a, Traces of estimated position, true fluorophore position, galvo (or piezo, slow scanner) position, and electro-optical deflector (EOD) position in an ideal case. The estimated position quickly converges to the true fluorophore position. **b,** In the case of imprecise scouting (a Gaussian estimator with $\sigma = 80$ nm), our initial guess is far from the true fluorophore position, and often it takes many iterations to converge. **c,** In the case of localizing a 100 nm bead, the size of the bead causes a blurring of the PSF and increases the intensity at the center, which leads to a bias in the estimator and slow convergence of the estimator to the centroid position of the bead. **d,** In the case of high background (30 kHz), the resulting bias in the estimator will lead to a similar slow convergence. Shown are instructive example tracks. Creeping is stochastic with a high variability, thus even in case of imperfections, a fraction of tracks converged quickly.

In all simulations, a fluorophore was placed at (200, 50, 0) nm and was localized with the 2D tracking sequence, Tracking_2D.json. Simple 2D Gaussian (see Methods Eq. 13 Linearized Least Squares Estimator) and donut (see Methods Eq. 8 Balzarotti et al.[1], Eq. S50) estimators were used. See example 3 (example3_Abberior_sequence.m or .ipynb).

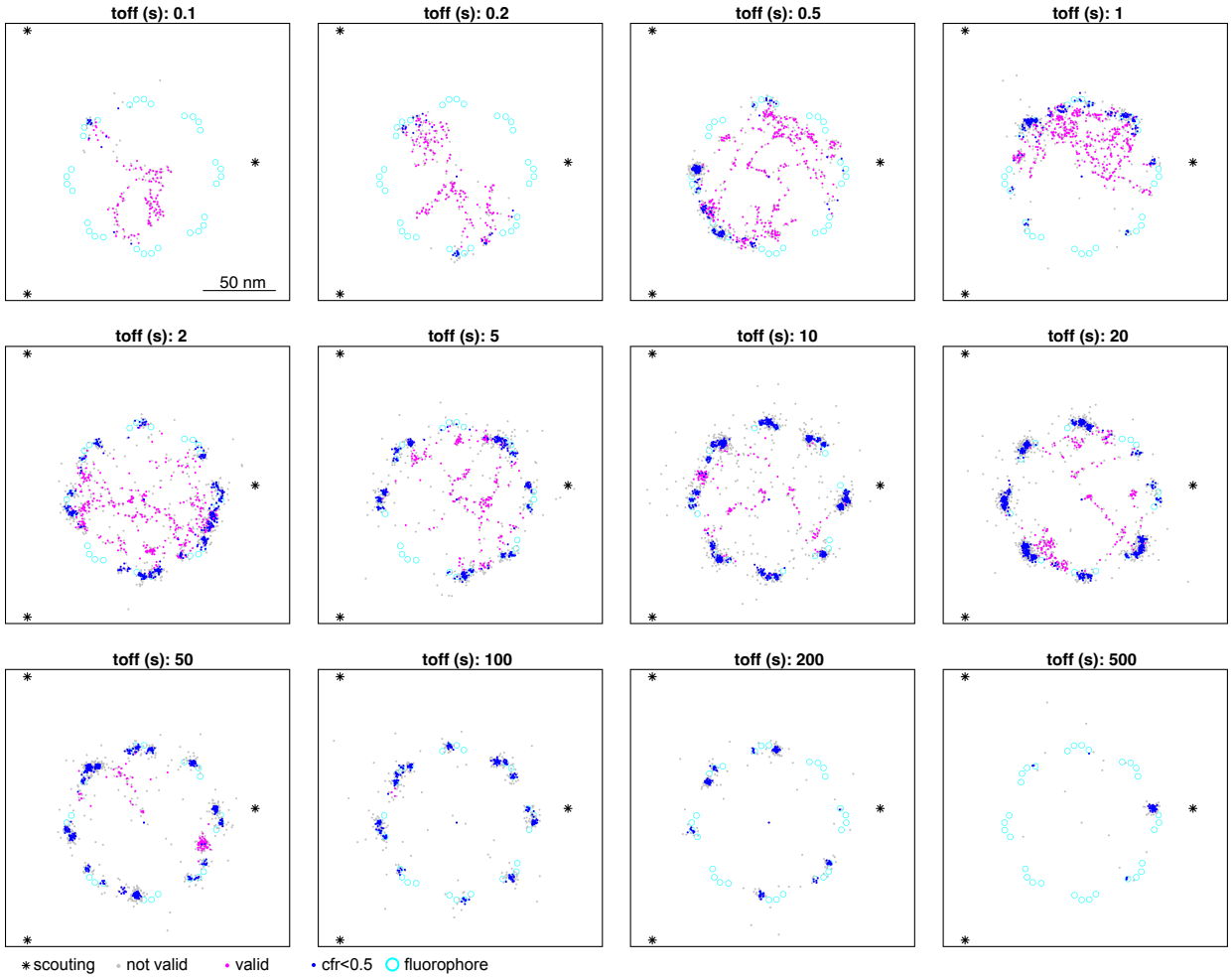

Supplementary Fig. 8. Optimizing fluorophore density. Effects of the off time of the dSTORM probe on localization density. Short off times result in many fluorophores being on at once, which means the sparsity requirement is not met. This leads to wrong localizations and prevents the CFR check (see Methods, Abberior MINFLUX model) from passing. Long off times results in most fluorophores being off when scouting or localization occurs and so they are never seen in the limited measurement time. For all experiments, we used a photon budget 5000, 2 reactivations, an Abberior 2D imaging sequence, Imaging_2D.json, and a measurement time of 60 s. See example 10 (example10_imaging.m or .ipynb).

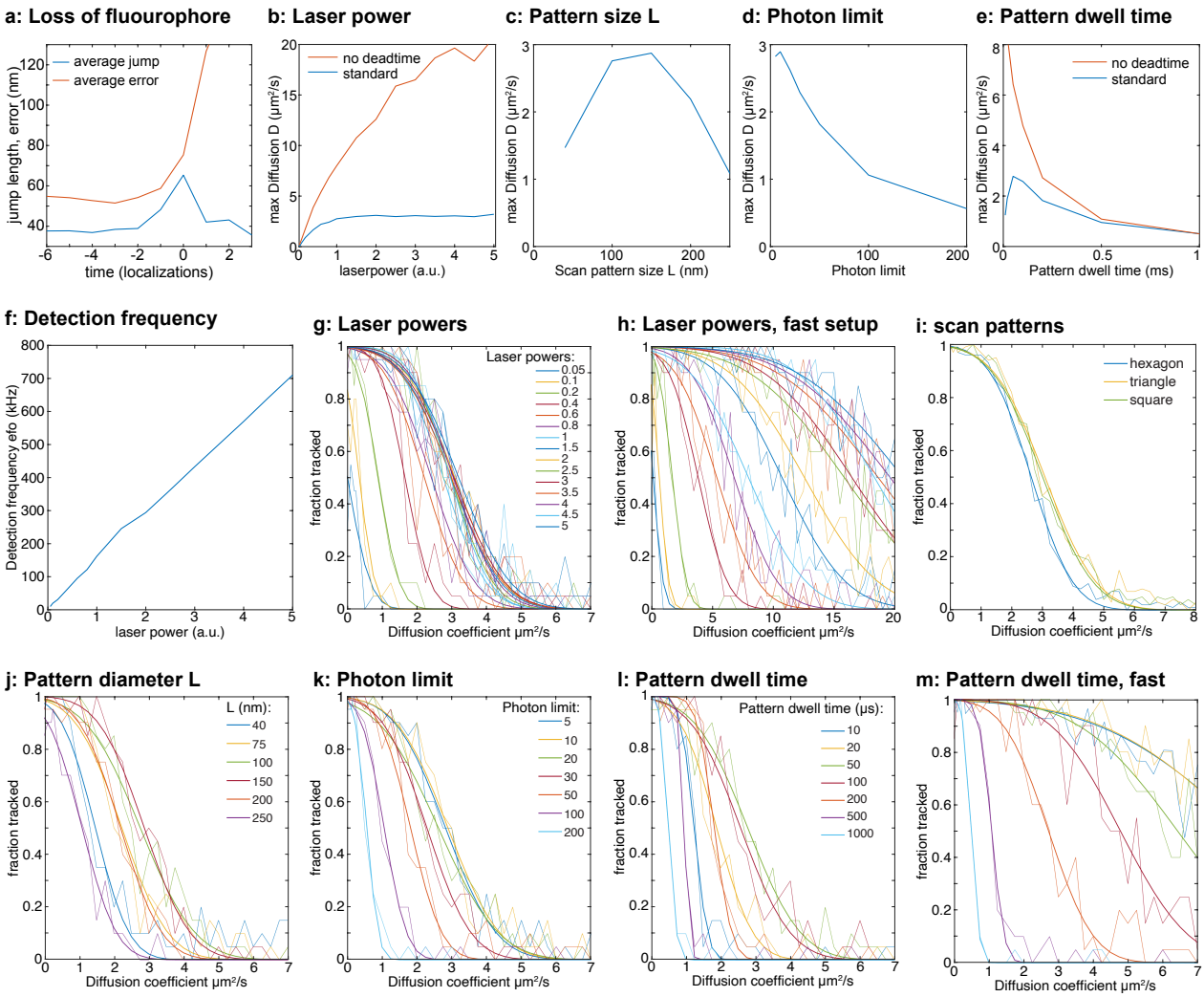

Supplementary Fig. 9. Optimizing a MINFLUX tracking experiment in silico. a, Jump length and localization error aligned by the last tracked localization and averaged over 300 tracks, shows that tracking fails after large random displacements. **b-e**, Systematic analysis of the maximum diffusion coefficient $D_{\max}$ (µm/s^2) that can be measured for different laser powers, pattern sizes, photon limits and pattern dwell times for the standard Abberior MINFLUX and for an equivalent microscope with no dead times. $D_{\max}$ increases with the laser power, but levels off quickly because of the limited time resolution of standard instruments. Note that high laser powers lead to high count rates of the fluorophores (**f**), which might become unrealistic. **g-m**, Fraction of successfully tracked molecules (defined as >90 consecutive localizations with an error below 100 nm) vs. the diffusion coefficient and sigmoidal fit. For each diffusion coefficient 20 tracks were simulated.

After choosing optimal values based on these parameter scans and optimal scan patterns, while keeping the same fluorophore emission rates, we could improve $D_{\max}$ from 2.5 µm^2/s to 4.2 µm^2/s (see Figure 2l, example 11, example11_max_diffusion.m or .ipynb).